Letter

Coupling Broadband Terahertz Dipoles to Microscale Resonators

Christopher Rathje, Rieke von Seggern, Leon A. Gräper, Jana Kredl, Jakob Walowski,
Markus Münzenberg, and Sascha Schäfer*

Read Online

ACCESS | 📊 Metrics & More | 📖 Article Recommendations | 🆂🅸 Supporting Information

ABSTRACT: Optically driven spintronic emitters are a unique class of terahertz (THz) sources due to their quasi-two-dimensional geometry and thereby their capability to effectively couple to resonator near fields. Global excitation of the emitters often obstructs the intricate details of the coupling mechanisms between local THz dipoles and the individual modes of resonator structures. Here, we demonstrate the spatial mapping of the coupling strength between a micrometer-scale terahertz source on a spintronic emitter and far-field light mediated by a structured metallic environment. For a bow-tie geometry, experimental results are reproduced by a numerical model, providing insights into the microscopic coupling mechanisms. The broad applicability of the technique is showcased by extracting the THz mode structure in split-ring resonator metasurfaces and linear arrays. With these developments, planar THz sources with tailored spectral and angular emission profiles become accessible.

KEYWORDS: spintronic THz emitter, split-ring resonator, bow-tie resonator, photonic mode mapping, electro-optic sampling, localized excitation
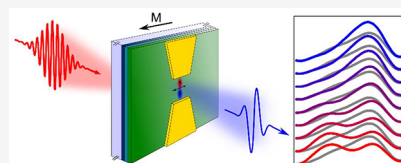
INTRODUCTION

The introduction of spintronic terahertz emitters (STEs)[1,2] consisting of stacks of ultrathin ferromagnetic and non-magnetic layers opened up a new class of pulsed terahertz (THz) sources, exhibiting ultrabroad and gapless emission spectra. In these emitters, a spin-polarized current is launched by femtosecond optical excitation within the magnetic layer and is subsequently deflected by the inverse spin Hall effect in a transverse direction orthogonal to the local spin polarization. The generated transient electric dipole emits broadband THz radiation into the far field.

In terms of THz emission efficiency of spintronic sources, many improvements over the original design have been achieved in recent years,[3−7] optimizing the layer config-uration,[8,9] film thicknesses,[2,9−14] material compositions and crystallinity,[2,11,12,15] and thin-film interfaces.[16−18] The depend-ence of the inverse spin Hall deflection on the local magnetization enables the control of the THz polarization state and even polarization patterns by tuning the magnet-ization profile of the emitter.[19−23] Similarly, in situ tuning of the thin-film strain induced by an adjacent biased ferroelectric material was demonstrated modifying the emitted THz field strength and the shape of the THz transient.[24,25] In other applications, the generated transverse current pulse is directly utilized and, for example, coupled into planar waveguides.[26]

Furthermore, the quasi-two-dimensional geometry of the emitter allows for a direct emitter patterning[9,22,23,27−31] or a coupling of the emitter surface to metallic microstructures[32,33] and metasurfaces,[34,35] aiming for a spectral and angular tuning of the emitted radiation, an improved excitation[36] or outcoupling efficiency,[37] or enhanced sensitivity in local THz spectroscopy.[38] Up to now, spectral tunability by employing

two-dimensional resonators and antennas combined with large-area illumination of the spintronic emitter yielded only moderate effects.

As a prerequisite for the successful design of patterned STEs, an understanding of the microscopic coupling of local THz dipoles to a photonic environment is essential. On the experimental side, several methodologies have been developed to locally map the material response in the THz frequency range, such as laser-induced THz emission microscopy[39−43] and THz- and mid-infrared variants of scanning near-field optical microscopy (SNOM).[44−47] These, however, were not yet been applied for characterizing the THz photonic environment within individual microstructures.

Here, we demonstrate the microscale mapping of coupling strengths between resonator structures and metasurfaces and subwavelength localized THz dipoles on spintronic emitters. Utilizing microscale bow-tie geometries excited by 16-μm-sized optical foci, we observe pronounced changes in the emitted THz spectrum. Numerical simulations link these findings to antenna resonances mediating the localized dipole and far-field radiation. For split-ring resonator metasurfaces, a spatially periodic spectral modulation is observed, which can be decomposed into individual modes. These developments allow for in-depth experimental tailoring and characterization
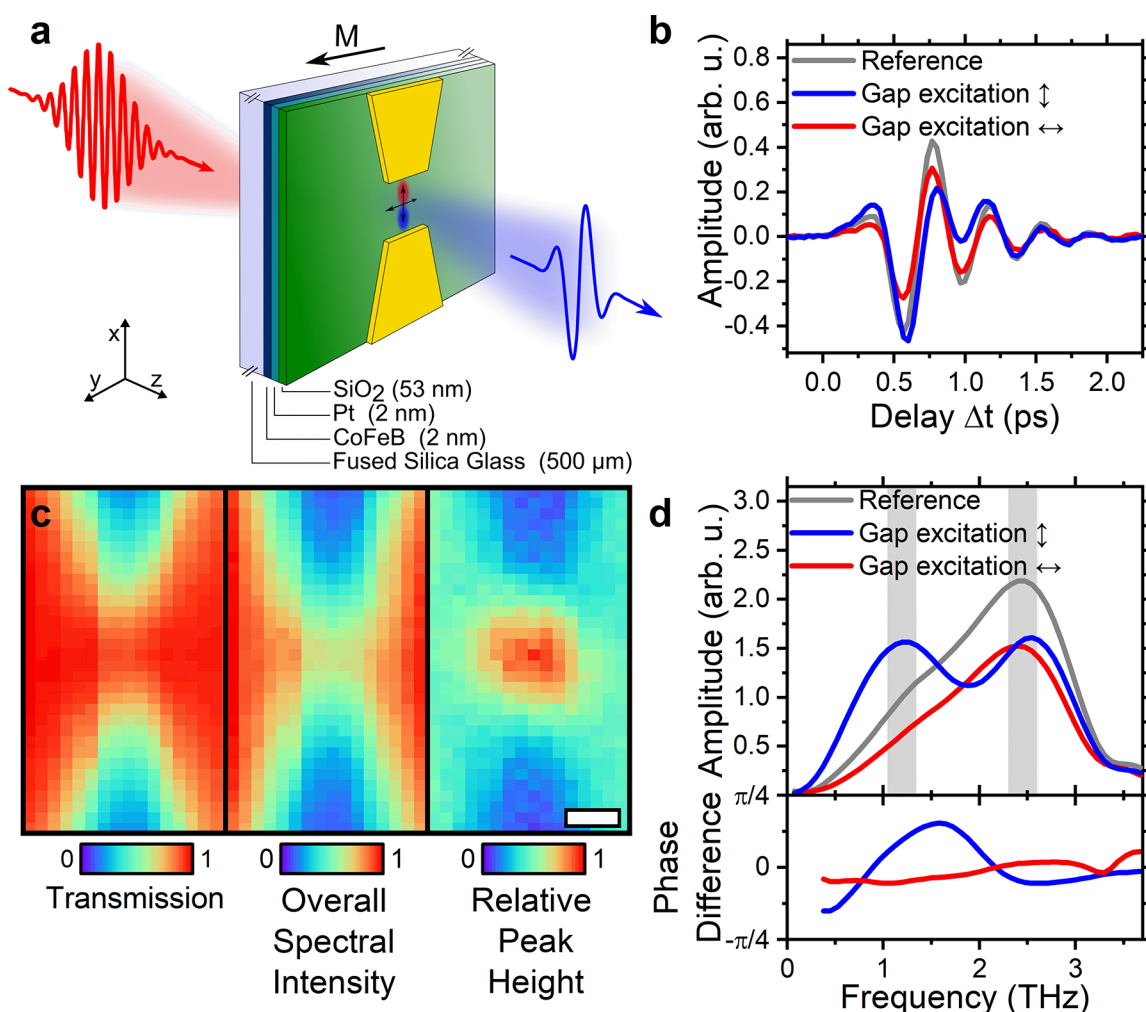
Figure 1. Tailoring terahertz emission spectra by surface microstructuring. (a) Experimental scheme. A localized THz electric dipole, driven by an optically triggered inverse spin Hall current, is coupled to the gap of a bow-tie resonator (sample magnetization: y-direction; THz polarization: x-direction). The emitted THz radiation is detected in the far field by electro-optic sampling. (b, d) THz time-domain signal (b) and corresponding spectral intensity (d) obtained for a bow-tie-coupled THz dipole (blue curves) and for an unstructured emitter area (gray curves). The pronounced changes in the emitted THz radiation for the bow-tie-coupled case vanish for the THz dipole polarization perpendicular to the bow-tie axis (red curve in (d)). The difference between the spectral phases for both polarizations with respect to the reference is shown in the lower panel. (c) Spatial map of the optical transmission (left) and overall spectral intensity of the emitted THz radiation (center) were recorded simultaneously by raster scanning the optical excitation spot (spectral intensity normalized to maximum). The intensity ratio of the two spectral regions highlighted in (d) weighted by the overall spectral intensity is displayed in the right panel, visualizing the strong confinement of dipole-bow-tie coupling within the gap region (scale bar: 10 μm).

of the THz photonic environment in close proximity to spintronic emitters.

RESULTS

For the generation of a micrometer-scale broadband THz emitter with a source size far below the THz diffraction limit, we utilize a resonator-grafted spintronic emitter bilayer (CoFeB(2 nm)/Pt(2 nm)), which is illuminated by a focused optical excitation pulse (70 fs fwhm pulse duration, 780 nm central wavelength, 16 μm fwhm spot size), as depicted in Figure 1a. The field polarization of the generated THz dipole is perpendicular to the local in-plane magnetization of the CoFeB layer and thereby tunable by the external magnetic field. The near field of the localized transient electric dipole is coupled to a metallic resonator structure in direct proximity to the emitter only separated by a SiO$_2$ (53 nm thickness) insulation layer.[33] For a varying position of the excitation focus, implemented by shifting the sample relative to the fixed optical beam, we detect

the emitted THz time-domain signal in the far field utilizing an electro-optic sampling approach (see Methods for details).

Local Dipole Coupled to a Bow-Tie Resonator. As a first example, we grafted a gold bow-tie antenna (10 μm gap size, 35 nm gold thickness, 5 nm thick chromium adhesion layer) onto the spintronic emitter. Placing the THz dipole far away from the resonator structure, and with the CoFeB magnetization perpendicular to the gap (Figure 1a), we observed a far-field transient (Figure 1b, gray curve) with a dominant oscillation period of about 0.5 ps. In the frequency domain, the resulting THz spectrum (Figure 1d, gray curve) shows a width of about 1.7 THz (fwhm), limited by the excitation pulse duration and the detection bandwidth, and a center-of-mass of 2.1 THz. Remarkably, the emitted THz signal changes drastically when the dipole is positioned within the gap of the bow tie (Figure 1b,d, blue curves). The emission spectrum now exhibits two maxima located at 1.2 and 2.55 THz, respectively, and an overall increased spectral bandwidth
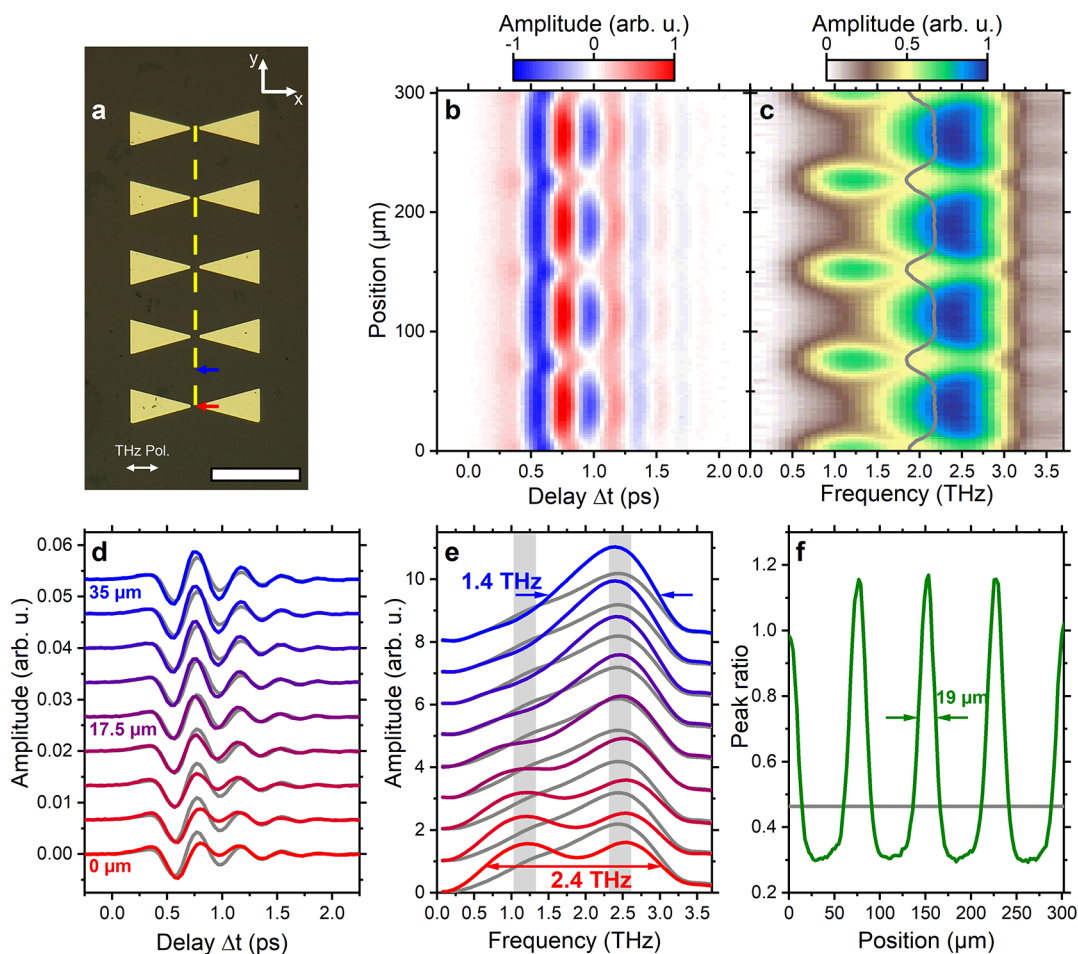
Figure 2. Coupling of a THz dipole to a bow-tie resonator array. (a) Optical micrograph of gold bow-tie antennas deposited on an STE (gap size: 10 μm, THz polarization perpendicular to gap, scale bar: 100 μm). (b, c) The position-dependent THz time-domain signal (b) and spectral intensity (c) recorded for an excitation pulse positioned along the yellow dashed line indicated in (a) show prominent variations and an additional resonance peak for in-gap excitation (step size 2.2 μm). Each THz spectrum is normalized to its integrated intensity. Spectral center-of-mass frequency is indicated by gray curve. (d, e) The exemplary selected time traces and (nonnormalized) spectra for electric dipole positions changing from in-gap (red curve; position indicated in a) to a point between two adjacent resonator structures (blue, cf. a) (gray curves: THz reference signal for unstructured emitter; spectral widths indicate fwhm). (f) The extracted ratio of the two spectral peaks (integrated over gray regions in (e)) shows a distinct spectral shift toward the lower frequency peak for dipole positions in the resonator gap (local confinement width of 19 μm fwhm).

of 2.4 THz. Importantly, and different from the results by applying spectral filter,[34] spectral amplitudes also exhibit an enhancement by about 55% around a frequency of 1.2 THz, indicating pronounced resonances. Changing the in-plane magnetization direction (and thereby the THz field polarization) by 90° uncouples the dipole from the bow-tie resonator, and the reference THz spectrum observed without a grafted resonator is largely recovered (Figure 1d, red curve). The differing coupling behavior for both polarizations is also found for the THz phase difference for emission from the bow-tie gap relative to the reference spectra (Figure 1d, lower panel).

To further extract the characteristic length scale of dipole-resonator coupling, we raster-scanned the position of the optical excitation focus relative to that of the resonator. In order to prevent a misalignment of the THz collection optics during scanning, the sample is moved, and the optics setup is kept constant. In Figure 1c, the resulting overall THz spectral intensity (central panel) and the normalized ratio of the 1.2 and 2.55 THz spectral components (right panel) are shown. As a spatial reference, the simultaneously recorded optical transmission of the pump light is depicted in the left panel.

The overall THz intensity is reduced by about 1 order of magnitude for the THz dipole located within the triangular gold region of the bow-tie resonator, which can be partially attributed to the THz transmission through the gold thin-film. Taking for simplicity, the transmission of an incident plane wave through a SiO$_2$/gold bilayer[48] together with the refractive indices of gold and SiO$_2$ at THz frequencies,[49,50] the transmittivity is estimated to be on the order of about 1.5%. Notably, the optical transmission in the gap almost equals the transmission in the reference region, ensuring that the excitation focus is not significantly clipped by the adjacent gold structure. Large spectral changes in the emitted THz radiation are visible only within a circular region in the gap with a diameter of about 20 μm, indicating the strongly localized interaction of the induced dipole with the surrounding metallic environment.

For investigating the spatial dependence of the emitted signal, its reproducibility, and coupling effects between adjacent antennas, we patterned a series of gold bow-tie resonators onto the STE surface (optical micrograph in Figure 2a) and recorded the THz emission for the optical focus being placed along a line through the resonator gaps (yellow dashed
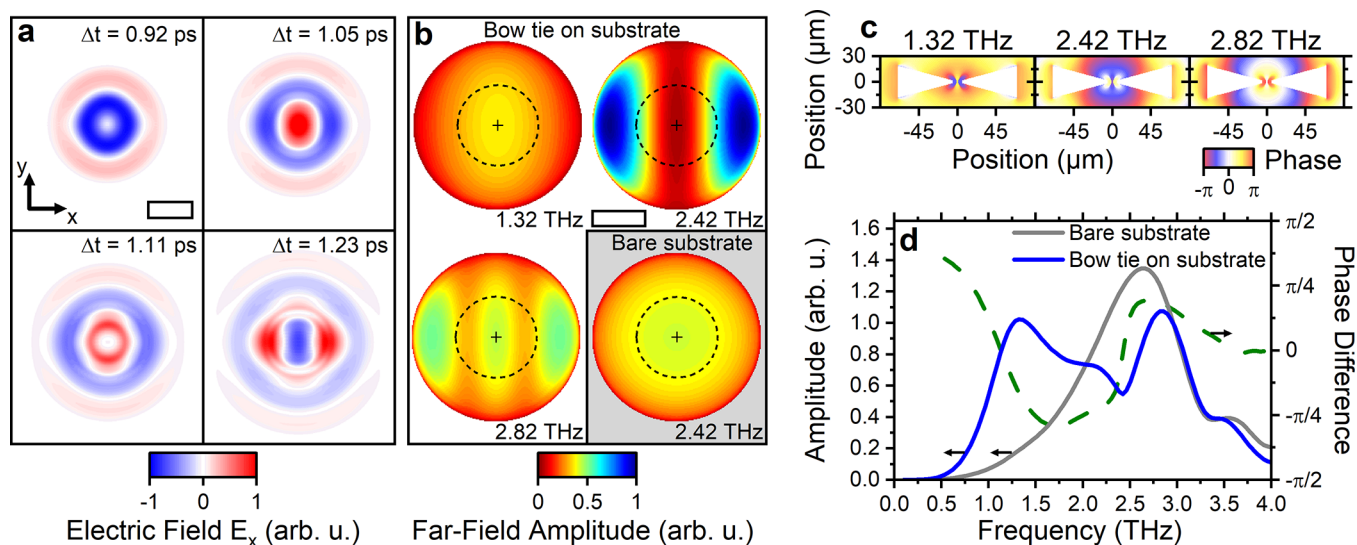
Figure 3. Finite-difference time-domain calculation of bow-tie-coupled dipole radiation. (a) Radiated electric field E_x for a localized dipole in the bow-tie gap evaluated at a 50 μm distant plane at different delay times (scale bar: 100 μm). (b) Extracted angular far-field emission pattern for three exemplary frequencies. As a reference, the corresponding pattern for the dipole above a bare substrate is given in the lower right panel (emission direction perpendicular to the substrate is indicated by cross mark; scale bar: $\frac{1}{2}\sqrt{k_x^2 + k_y^2}/k$; dotted circle: acceptance angle of the experimental detection unit). (c) Calculated wrapped near-field phase for the three exemplary frequencies in (b) provide a microscopic mechanism for the observed frequency-dependent angular emission changes (see text for details). (d) Simulated spectral intensity for a dipole in the bow-tie gap (blue curve) and above a bare substrate (gray curve), obtained by integrating the angularly resolved emission intensities in (b) within the acceptance angle. Green dashed curve: difference in the spectral phase for both cases.

line). Figure 2b,c illustrates the obtained THz time-domain signal and THz spectrum as a function of the optical excitation focus position, exhibiting pronounced changes in the emitted THz radiation. In the spectra, the center-of-mass oscillates between lower and higher frequency components (gray curve). A selection of time traces and spectra are shown in Figure 2d,e recorded with an excitation position ranging from in-gap (red) to in-between adjacent bow ties (blue). Notably, for an excitation between two bow ties, the total emitted intensity even exceeds the reference signal (intensity enhancement of about 23%), indicating an antenna-like effect of the triangular side-edges of the resonator. Here, the overall temporal and spectral shape of the THz transient shows only moderate changes compared to the reference pulse. Similar effects are observed in the vicinity of isolated bow-tie structures and at the out-most resonators in a linear array (see Figure S6). Figure 2f shows the ratio of spectral amplitudes, each integrated over the two gray marked areas in Figure 2e, as a function of the excitation position. The resulting feature width of 19 μm (fwhm) demonstrates the strong localization of the observed mode between the gold tips with low coupling efficiency in-between bow-ties.

Numerical Model of Dipole-Resonator Coupling. In order to develop a theoretical framework of the local dipole-resonator coupling, we conducted finite-difference time-domain (FDTD) simulations (ANSYS Lumerical FDTD module) of a single bow-tie antenna excited by a dipole centered in the bow-tie gap (see Methods for details). Due to the nanoscale scattering length of spin currents in metallic thin films, the spatial dimensions of the induced inverse spin Hall currents are negligible in comparison to the size of the antenna. The time-dependent dipole moment is chosen to be proportional to the experimental time-domain THz signal recorded on an unstructured surface (cf. Figure 1b, gray curve). Figure 3a displays the radiated electric field E_x in a

plane with a distance of 50 μm to the substrate for different delay times Δt. At early times (Δt = 0.92 ps), the electric field distribution shows an approximate circular symmetric phase as expected for the radiation pattern of an uncoupled dipole. At later times, a pronounced symmetry breaking in the radiation field can be observed, with the main axis linked to the orientation of the bow-tie antenna. From the field distribution close to the sample, we calculated the far-field emission pattern at different frequencies, as displayed in Figure 3b. The angular emission pattern exhibits distinct changes with frequency, gradually evolving from a rather homogeneous distribution (slightly elongated along the k_y-direction) at 1.32 THz to distributions with two and three lobes at 2.42 and 2.82 THz, respectively (see also Figure S4). As a comparison, we also calculated the far-field emission pattern of a dipole on a bare substrate, which is close to circular symmetry and shows no significant frequency dependence. Notably, the presence of a substrate already substantially modifies the far-field emission pattern as compared to a dipole in free space.[51] To obtain a microscopic understanding of the frequency-dependent angular emission patterns, Figure 3c provides the calculated electric near-field phase in the plane of the bow-tie resonator. At 1.32 THz the electric field in the bow-tie gap oscillates in-phase with the field at the base of the bow-tie triangles, resulting in constructive interference in the direction perpendicular to the surface. At 2.42 THz the field in the gap and base regions oscillate with a $\frac{4}{3}\pi$ phase difference so that the emission in the perpendicular direction interferes mainly destructively. At a frequency of 2.82 THz the different antenna parts oscillate with a phase difference of π, which yields a more complex angular far-field distribution. In the experiment, THz radiation is collected with a solid angle of 0.66 sr, corresponding to an opening angle of $\pm26.5°$, as defined by the first off-axis parabolic mirror after the sample.
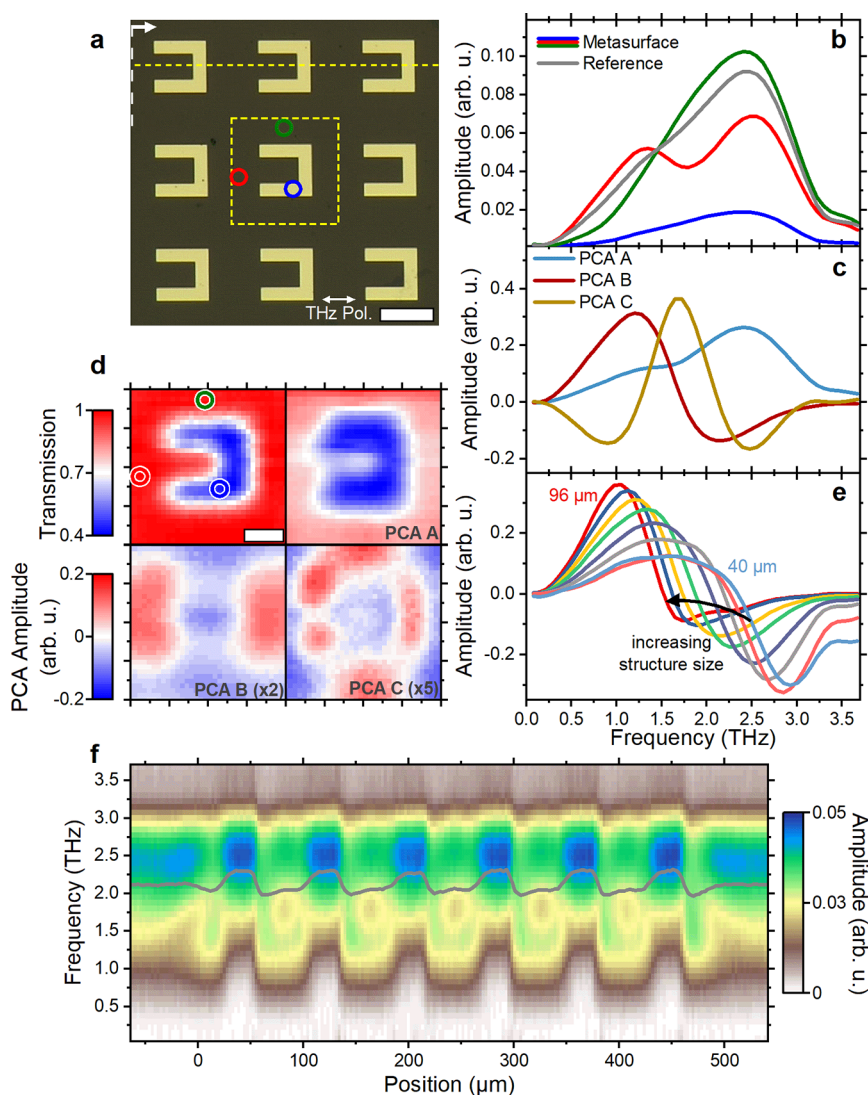
Figure 4. Mapping optical modes in metasurfaces by localized THz dipole excitation. (a) Optical micrograph of a two-dimensional gold split-ring resonator (SRR) array deposited onto a spintronic THz emitter (scale bar: 40 μm). (b) Exemplary THz spectra for the THz dipole placed at different positions in the unit cell of the metasurface. Line colors correspond to the locations indicated by open circles in (a). Gray curve: reference THz spectrum from an unstructured emitter. (c, d) Raster scanning of the optical excitation pulse position across an SRR unit cell, in the region indicated by the yellow dashed square in (a), yields a transmission map (d, upper left) and THz time-domain signals for each position (scale bar: 20 μm). A principal component analysis (PCA) decomposes the resulting spectra into three dominant spectral components (c) with corresponding coefficient maps (A) (d, top right), (B) (d, bottom left), and (C) (d, bottom right). (e) PCA spectral component (B) extracted for scaled metasurfaces with unit cells ranging from 40 to 96 μm yield a frequency-dependent shift of the maximum of PCA component. (f) THz spectra recorded along a line through an array of six resonator structures (scanning position (yellow dashed line) and zero-position (white dashed arrow) at left edge of first SRR unit cell both indicated in a) show significant spectral variations within the array and the presence of edge modes. Each spectrum is normalized to its integrated intensity. The corresponding THz time-domain signals are depicted in Figure S12. Gray curve: spectral center-of-mass.

To account for the angular selectivity of the setup, we only consider the central region in the far-field pattern indicated by dashed circles in Figure 3b. For the bow-tie-coupled dipole, the extracted overall spectral intensity in the central angular region (Figure 3d, blue curve) features two pronounced peaks at 1.32 and 2.82 THz and a minimum at 2.42 THz, reproducing the main features in the experimental spectrum (Figure 1d). Enhanced spectral intensities occur at frequencies with the angular emission distribution becoming localized around k = 0, yielding a more collimated radiation emitted perpendicular to the substrate. In contrast, at frequencies of about 2.42 THz the radiation is preferentially emitted with larger k_x-components not detected in the experiment. In contrast, the corresponding

spectral intensity extracted for the bare substrate (Figure 3d, gray curve) largely resembles that of the dipole excitation spectrum. Equally, the change in the spectral phase as observed experimentally (Figure 1d, lower panel) is qualitatively reproduced in the simulation, which, however, exhibits overall larger spectral phase shifts and steeper phase gradients (Figure 3d, green curve).

Due to computational size limitations, only a single antenna is considered. Therefore, the behavior for an excitation between two bow-tie antennas was not simulated.

THz Mode Mapping. Finally, we demonstrate that the coupling of a THz dipole with resonator structures can also be investigated in the case of more complex surface patterns. For

this purpose, a periodic array of gold split-ring resonators (SRRs)[52] was deposited onto a continuous spintronic emitter, as depicted in Figure 4. Similar to the case of bow-tie resonators, the emitted THz spectrum depends on the excitation position, as exemplified in Figure 4b for the three positions marked in Figure 4a. For isolated split-ring resonators only weak dipole couplings are found, highlighting the importance of SRR resonator couplings due to their larger mode volume as compared to the case of bow-tie antennas (cf. Figures S12 and S13). In order to illustrate the local emission changes, we performed an excitation raster scan within one unit cell of the array (indicated as square in Figure 4a) and decomposed the recorded spectral variations by a principal component analysis (PCA)[53] after subtracting the average spectrum within the scan range. The three dominant extracted PCA components (A)−(C), as well as a spatial map of the associated coefficients, are depicted in Figure 4c and d, respectively.

The PCA component (A) largely mirrors the reference spectrum and has high negative coefficients at regions with an overall attenuated emission, for example, at the gold-covered sample regions. The most distinct spectral change is detected close to the gap in the split-ring resonators (position indicated by an open red circle), at which large coefficients for PCA component (B) are obtained. In particular, the exemplary spectrum exhibits an additional peak around 1.35 THz which corresponds to the dispersive line-shape in the PCA component (B). A spectrally and spatially distinct mode (component (C)) is located predominantly between SRRs in the vertical direction and, for example, results in a dip at around 1.8 THz in the THz emission spectrum at the position indicated by the open red circle.

The expected size dependence of the resonance in the (B) component is experimentally verified by investigating THz emission from rescaled SRR arrays with unit cells ranging from 40 to 96 μm (Figure 4e). Generally speaking, the extracted PCA components are expected to be related to photonic Bloch modes[54] in the periodic SRR array and their coupling to far-field radiation within the acceptance angle of the THz detection setup. In similar geometries, previous experiments with patterned GaAs-based optical rectification sources have indicated a spatial dependence of the THz spectrum on the excitation position in split-ring resonator arrays.[43] Furthermore, a single THz resonance in such a structure was also recently identified by utilizing scattering SNOM with narrow bandwidth excitation.[55]

To highlight the difference between THz modes within a periodic array and at the array edges, we performed a line scan of the optical excitation spot across a 6 × 6 SRR array, as indicated by the yellow dashed line in Figure 4a. The corresponding THz spectra are listed in Figure 4f. Within the array, the spectral changes as extracted from PCA are recovered. In addition, at the positions smaller zero or larger than 480 μm edge states are apparent. Notably, the low symmetry of the SRR unit cell along the scan direction is also evident in a spatial shift of the spectral intensity minimum at 1.8 THz by about 7 μm toward the gap side of the split-ring resonator, resulting in staggered configuration and a slight difference between the left and right edge state. In future studies, the relationship between properties of the emitted THz radiation and the topological character of the photonic edge state[56,57] could be of particular interest.

In this paper, we chose bow-ties and SRRs as established and simple two-dimensional photonic building-blocks. When utilizing our findings for constructing, for example, high-brightness THz emitters or structures with an intense local THz-field strength, we expect that more advanced geometries might be useful. Nevertheless, the THz emission modulated by the simpler structures selected in our work already contains considerable complexity, which would need to be addressed by further theoretical work.

■ CONCLUSION AND OUTLOOK

In conclusion, we have investigated the emission properties of locally excited micropatterned spintronic THz emitters. By grafting metallic structures onto the emitter surface, we demonstrated the flexible tailoring of spectral emission properties, exhibiting a significant spectral enhancement at distinct frequency components. Employing localized THz dipole excitation allows for a direct coupling to THz near fields, which we utilized for the mapping of THz modes in metasurfaces. Since the THz source can be chosen to be much smaller than the THz wavelength, also optically dark modes or modes with small mode volumes are accessible, so that our approach should yield a more comprehensive picture of the THz photonic environment as compared to global excitation of the structure. Potential applications include the characterization of topological THz systems, as well as the generation of high near-field strengths in microresonators.

■ METHODS

Experimental Setup. The experiments were carried out in an optical THz spectroscopy setup (cf., Figure S1a). Short infrared laser pulses from a frequency-doubled erbium-doped femtosecond fiber laser (pulse duration: 70 fs (fwhm), wavelength: 780 nm; repetition rate: 100 MHz; C-Fiber 780 from Menlo Systems) were focused onto the structured spintronic terahertz emitter sample (16 μm fwhm focal spot size, pulse energy: 0.4 nJ) under a dry-nitrogen atmosphere. The external magnetic field of a pair of neodymium magnets saturates the in-plane magnetization of the STE. The THz transient was detected in an electro-optic sampling setup.[58,59] Here, the THz pulse induces birefringence in a 500 μm thick ⟨110⟩-oriented ZnTe electro-optic crystal proportional to the instantaneous electric field, rotating the polarization of a probing pulse. Its polarization state for different time delays of the THz and probing pulse was recorded behind a Wollaston prism using balanced photodiodes. For obtaining a higher signal-to-noise ratio, a lock-in amplification was applied with an optical chopper wheel installed in the excitation pulse arm (modulation frequency: 140 Hz). For automated raster scanning, the emitter position was controlled by a three-axis piezo-motor-driven translation stage system.

The detection angle sensitivity of our setup is limited to approximately ±26.5° due to the collection angle of the off-axis parabolic mirror located after the spintronic terahertz emitter (Figure S1b). A silicon wafer tilted to the THz Brewster angle transmits the p-polarized THz transient and reflects the residual 780 nm beam onto a photodiode detector. In this configuration, we recorded the optical transmission at each excitation pulse position during the recording of the THz time-domain scans.

For the experiments reported here, the magnetic field was oriented in the vertical direction to maintain p-polarized THz

emission. The relative orientation between the THz polarization direction and the microstructures was adjusted by rotation of the emitter.

For obtaining the emitted THz spectra, acquired delay-dependent electro-optic sampling signals are filtered by a super-Gaussian window function (width: 2.5 ps fwhm) to exclude trailing replica pulses (resulting from reflections at optical components) from the analysis. In addition, we applied zero padding of the time-domain signal before performing a Fourier transform of the signal.

Sample Preparation. We utilize a spintronic terahertz emitter consisting of a 2 nm thin ferromagnetic CoFeB layer and a 2 nm thin nonmagnetic Pt layer on fused silica glass. The CoFeB layer is magnetron sputtered onto the substrate, directly followed by the Pt layer being deposited by e-beam evaporation without breaking the vacuum conditions in a separate ultrahigh-vacuum chamber with a base pressure of 5×10^{-10} mbar. To avoid direct injection of electron currents from the spintronic bilayer into the microresonator structures, the bilayer was capped by an insulating SiO_2 layer (thickness: 53 nm).

For the addition of gold structures onto the spintronic emitter, electron-beam lithography (EBL) was employed. A double-layer positive resist film (PMMA E-Beam Resist AR-P 632.06 (50K) and AR-P 672.03 (950 K) from Allresist) was subsequently spin-coated (2000 rpm, with 3 min of heating at 150 °C) onto the emitter. Electron beam exposure was carried out in a Helios NanoLab 600i (FEI) equipped with an EBL module (ELPHY-Quantum (Raith)) at a dose of about 150 $\mu C/cm^2$ and an electron kinetic energy of 20 keV and beam current of 0.34 nA.

The exposed sample was developed for 1 min (E-Beam Developer AR 600−55 from Allresist) and transferred into an electron-beam evaporator (Pfeiffer Vacuum PLS 500) where 35 nm gold was deposited with a 5 nm chromium adhesion layer. Subsequently, the lift-off of residual resist was performed in an acetone bath, resulting in isolated gold microresonators grafted on the emitter surface.

Resonator Geometries. In our studies, we examined three different gold bow-tie antenna designs deposited onto the spintronic THz emitter surface, with the sizes scaled evenly (cf. Figure S3a). In addition to the structures mentioned in the main text[60] (length $l_1 = 140$ μm, height $h_1 = 37.5$ μm, gap size $g_1 = 10$ μm), bow-tie structures with geometrical dimensions of $l_2 = 70$ μm, $h_2 = 18.75$ μm, $g_2 = 5$ μm and $l_3 = 210$ μm, $h_3 = 56.3$ μm, $g_3 = 15$ μm were investigated. The split-ring resonators mapped in Figure 4 of the main text have the dimensions of gap size $g = 20$ μm, wire width $w = 10$ μm, length $l = 40$ μm, and unit cell size = 80 μm (cf. Figure S3b). Additionally, the size of the split-ring resonator arrays was varied from $l = 20-48$ μm in 4 μm increments ($g = l/2$, $w = l/4$, and unit cell = $2l$).

Numerical Simulations. To obtain a microscopic understanding of the dipole-resonator coupling, we carried out numerical finite-difference time-domain simulations of the electric dipole coupling to a bow-tie antenna using a commercial software package (ANSYS Lumerical FDTD module). In a three-dimensional simulation geometry, a gold bow-tie structure (thickness: 35 nm) is placed on top of a SiO_2 substrate (thickness: 100 μm). We applied the Drude model to approximate the dielectric properties of gold at terahertz frequencies (plasma frequency: 1.38×10^{16} rad/s; permittivity: 1, plasma collision frequency: 4×10^{13} rad/s[61]). The

experimentally recorded time-domain signal (cf. Figure 1b) is used as a source signal for an electric point-dipole positioned in the bow-tie gap near the substrate−air interface (10 nm displaced from the interface, polarization in x-direction). At the simulation box boundaries, perfectly matched layers are applied to avoid back reflections of the electromagnetic waves. The temporal and spatial THz field distribution is recorded in a plane just above the dipole, as well as in a plane at $z = 50$ μm. After applying an apodization to exclude residual back reflections from the simulation boundaries, the spectral THz components are extracted using a temporal Fourier transformation.

For the calculation of the frequency-dependent far field,[62] the recorded field distribution in the 50 μm plane was used. A spatial window function was employed to avoid electric field truncation at the edges of the sampling plane (far-field filter setting: $\alpha = 0.05$). The phase of the electric near-field was extracted from a temporal Fourier transformation of the electric field calculated in the bow-tie antenna plane. To obtain the overall spectral intensity as depicted in Figure 3d, we only considered the central portion of the far field with an effective radius of $\pm 26.5°$, equal to the experimental THz detection angle.

■ ASSOCIATED CONTENT

Data Availability Statement

The data that support the plots within this paper and other findings of this study are available from the corresponding author on reasonable request.

Ⓢ Supporting Information

The Supporting Information is available free of charge at https://pubs.acs.org/doi/10.1021/acsphotonics.3c00833.

> Details of experimental setup; Further information regarding the sample homogeneity and resonator geometries; Numerical simulation results for the THz far field; Additional experimental results for bow ties of different sizes and comparison between isolated bow tie and bow-tie array; THz mode mapping for a single split ring, closed rings, and rotated open split rings (PDF)

■ AUTHOR INFORMATION

Corresponding Author

Sascha Schäfer − *Institute of Physics, University of Oldenburg, 26129 Oldenburg, Germany; Department of Physics and Regensburg Center for Ultrafast Nanoscopy, University of Regensburg, 93053 Regensburg, Germany;* Email: sascha.schaefer@ur.de

Authors

Christopher Rathje − *Institute of Physics, University of Oldenburg, 26129 Oldenburg, Germany*

Rieke von Seggern − *Institute of Physics, University of Oldenburg, 26129 Oldenburg, Germany; Department of Physics, University of Regensburg, 93053 Regensburg, Germany;* ⓞ orcid.org/0009-0008-5080-9672

Leon A. Gräper − *Institute of Physics, University of Oldenburg, 26129 Oldenburg, Germany*

Jana Kredl − *Institute of Physics, University of Greifswald, 17489 Greifswald, Germany*

Jakob Walowski − *Institute of Physics, University of Greifswald, 17489 Greifswald, Germany*

Markus Münzenberg − *Institute of Physics, University of Greifswald, 17489 Greifswald, Germany*

Complete contact information is available at:
https://pubs.acs.org/10.1021/acsphotonics.3c00833

■ REFERENCES

(1) Kampfrath, T.; et al. Terahertz spin current pulses controlled by magnetic heterostructures. *Nat. Nanotechnol.* **2013**, *8*, 256−260.

(2) Seifert, T.; et al. Efficient metallic spintronic emitters of ultrabroadband terahertz radiation. *Nat. Photonics* **2016**, *10*, 483−488.

(3) Bull, C.; Hewett, S. M.; Ji, R.; Lin, C.-H.; Thomson, T.; Graham, D. M.; Nutter, P. W. Spintronic terahertz emitters: Status and prospects from a materials perspective. *APL Mater.* **2021**, *9*, 90701.

(4) Papaioannou, E. T.; Beigang, R. THz spintronic emitters: a review on achievements and future challenges. *Nanophotonics* **2021**, *10*, 1243−1257.

(5) Wu, W.; Yaw Ameyaw, C.; Doty, M. F.; Jungfleisch, M. B. Principles of spintronic THz emitters. *J. Appl. Phys.* **2021**, *130*, 91101.

(6) Seifert, T. S.; Cheng, L.; Wei, Z.; Kampfrath, T.; Qi, J. Spintronic sources of ultrashort terahertz electromagnetic pulses. *Appl. Phys. Lett.* **2022**, *120*, 180401.

(7) Feng, Z.; Qiu, H.; Wang, D.; Zhang, C.; Sun, S.; Jin, B.; Tan, W. Spintronic terahertz emitter. *J. Appl. Phys.* **2021**, *129*, 10901.

(8) Feng, Z.; et al. Highly Efficient Spintronic Terahertz Emitter Enabled by Metal-Dielectric Photonic Crystal. *Adv. Opt. Mater.* **2018**, *6*, 1800965.

(9) Yang, D.; et al. Powerful and Tunable THz Emitters Based on the Fe/Pt Magnetic Heterostructure. *Adv. Opt. Mater.* **2016**, *4*, 1944−1949.

(10) Torosyan, G.; Keller, S.; Scheuer, L.; Beigang, R.; Papaioannou, E. T. Optimized Spintronic Terahertz Emitters Based on Epitaxial Grown Fe/Pt Layer Structures. *Sci. Rep.* **2018**, *8*, 1311.

(11) Zhang, S.; Jin, Z.; Zhu, Z.; Zhu, W.; Zhang, Z.; Ma, G.; Yao, J. Bursts of efficient terahertz radiation with saturation effect from metal-based ferromagnetic heterostructures. *J. Phys. D: Appl. Phys.* **2018**, *51*, 034001.

(12) Wu, Y.; et al. High-Performance THz Emitters Based on Ferromagnetic/Nonmagnetic Heterostructures. *Adv. Mater.* **2017**, *29*, 1603031.

(13) Seifert, T. S.; et al. Terahertz spectroscopy for all-optical spintronic characterization of the spin-Hall-effect metals Pt, W and Cu 80 Ir 20. *J. Phys. D: Appl. Phys.* **2018**, *51*, 364003.

(14) Qiu, H. S.; et al. Layer thickness dependence of the terahertz emission based on spin current in ferromagnetic heterostructures. *Opt. Express* **2018**, *26*, 15247−15254.

(15) Sasaki, Y.; Suzuki, K. Z.; Mizukami, S. Annealing effect on laser pulse-induced THz wave emission in Ta/CoFeB/MgO films. *Appl. Phys. Lett.* **2017**, *111*, 102401.

(16) Gueckstock, O.; et al. Terahertz Spin-to-Charge Conversion by Interfacial Skew Scattering in Metallic Bilayers. *Adv. Mater.* **2021**, *33*, 2006281.

(17) Nenno, D. M.; et al. Modification of spintronic terahertz emitter performance through defect engineering. *Sci. Rep.* **2019**, *9*, 13348.

(18) Li, G.; et al. THz emission from Co/Pt bilayers with varied roughness, crystal structure, and interface intermixing. *Phys. Rev. Mater.* **2019**, *3*, No. 084415.

(19) Hibberd, M. T.; Lake, D. S.; Johansson, N. A. B.; Thomson, T.; Jamison, S. P.; Graham, D. M. Magnetic-field tailoring of the terahertz polarization emitted from a spintronic source. *Appl. Phys. Lett.* **2019**, *114*, 31101.

(20) Niwa, H.; Yoshikawa, N.; Kawaguchi, M.; Hayashi, M.; Shimano, R. Switchable generation of azimuthally- and radially-polarized terahertz beams from a spintronic terahertz emitter. *Opt. Express* **2021**, *29*, 13331.

(21) Kong, D.; et al. Broadband Spintronic Terahertz Emitter with Magnetic-Field Manipulated Polarizations. *Adv. Opt. Mater.* **2019**, *7*, 1900487.

(22) Schulz, D.; Schwager, B.; Berakdar, J. Nanostructured Spintronic Emitters for Polarization-Textured and Chiral Broadband THz Fields. *ACS Photonics* **2022**, *9*, 1248−1255.

(23) Liu, C.; et al. Active spintronic-metasurface terahertz emitters with tunable chirality. *Adv. Photon.* **2021**, *3*, No. 056002.

(24) Agarwal, P.; Huang, L.; Ter Lim, S.; Singh, R. Electric-field control of nonlinear THz spintronic emitters. *Nat. Commun.* **2022**, *13*, 4072.

(25) Cheng, H.; et al. Giant Electrical Modulation of Terahertz Emission in Pb(Mg1/3 Nb2/3)0.7 Ti0.3 O3/Co−Fe−B/Pt Structure. *Phys. Rev. Appl.* **2021**, *16*, No. 054011.

(26) Hoppe, W.; et al. On-Chip Generation of Ultrafast Current Pulses by Nanolayered Spintronic Terahertz Emitters. *ACS Appl. Nano Mater.* **2021**, *4*, 7454−746.

(27) Song, B.; et al. Controlling terahertz radiation with subwavelength blocky patterned CoFeB/Pt heterostructures. *Appl. Phys. Express* **2019**, *12*, 122003.

(28) Jin, Z.; et al. Terahertz Radiation Modulated by Confinement of Picosecond Current Based on Patterned Ferromagnetic Heterostructures. *Phys. Status Solidi RRL* **2019**, *13*, 1900057.

(29) Wu, W.; Lendinez, S.; Taghipour Kaffash, M.; Schaller, R. D.; Wen, H.; Jungfleisch, M. B. Modification of terahertz emission spectrum using microfabricated spintronic emitters. *J. Appl. Phys.* **2020**, *128*, 103902.

(30) Talara, M.; et al.. Efficient terahertz wave generation of diabolo-shaped Fe/Pt spintronic antennas driven by a 780 nm pump beam. *Appl. Phys. Express* **2021**, *14*, 042008.

(31) Tong, M.; et al.. Light-Driven Spintronic Heterostructures for Coded Terahertz Emission. *ACS Nano* **2022**, *16*, 8294−8300.

(32) Nandi, U.; Abdelaziz, M. S.; Jaiswal, S.; Jakob, G.; Gueckstock, O.; Rouzegar, S. M.; Seifert, T. S.; Klaui, M.; Kampfrath, T.; Preu, S. Antenna-coupled spintronic terahertz emitters driven by a 1550 nm femtosecond laser oscillator. *Appl. Phys. Lett.* **2019**, *115*, 22405.

(33) Stiewe, F.-F.; et al. Spintronic emitters for super-resolution in THz-spectral imaging. *Appl. Phys. Lett.* **2022**, *120*, 32406.

(34) Liu, Y.; et al. Generation of tailored terahertz waves from monolithic integrated metamaterials onto spintronic terahertz emitters. *Nanotechn.* **2021**, *32*, 105201.

(35) Sun, Y.; et al. Flexible Control of Broadband Polarization in a Spintronic Terahertz Emitter Integrated with Liquid Crystal and Metasurface. *ACS Appl. Mater. Interfaces* **2022**, *14*, 32646−32656.

(36) Liu, S.; et al. Nanoplasmonic-Enhanced Spintronic Terahertz Emission. *Adv. Mater. Interfaces* **2022**, *9*, 2101296.

(37) Shahriar, B. Y.; Carnio, B. N.; Hopmann, E.; Elezzabi, A. Y. Enhanced directive terahertz radiation emission from a horn antenna-coupled W/Fe/Pt spintronic film stack. *Appl. Phys. Lett.* **2021**, *119*, 92402.

(38) Bai, Z.; et al. Near-field Terahertz Sensing of HeLa Cells and Pseudomonas Based on Monolithic Integrated Metamaterials with a Spintronic Terahertz Emitter. *ACS Appl. Mater. Interfaces* **2020**, *12*, 35895−3590.

(39) Tonouchi, M.; Yamashita, M.; Hangyo, M. Terahertz radiation imaging of supercurrent distribution in vortex-penetrated YBa2-Cu3O7−δ thin film strips. *J. Appl. Phys.* **2000**, *87*, 7366−7375.

(40) Kiwa, T.; Tonouchi, M.; Yamashita, M.; Kawase, K. Laser terahertz-emission microscope for inspecting electrical faults in integrated circuits. *Opt. Lett.* **2003**, *28*, 2058−2060.

(41) Klarskov, P.; Kim, H.; Colvin, V. L.; Mittleman, D. M. Nanoscale Laser Terahertz Emission Microscopy. *ACS Photonics* **2017**, *4*, 2676−2680.

(42) Li, P.; Liu, S.; Liu, Z.; Li, M.; Xu, H.; Xu, Y.; Zeng, H.; Wu, X. Laser terahertz emission microscopy of nanostructured spintronic emitters. *Appl. Phys. Lett.* **2022**, *120*, 201102.

(43) Serita, K.; Darmo, J.; Kawayama, I.; Murakami, H.; Tonouchi, M. Direct Measurements of Terahertz Meta-atoms with Near-Field Emission of Terahertz Waves. *J. Infrared Milli Terahz Waves* **2017**, *38*, 1107−1119.

(44) Chen, H.-T.; Kersting, R.; Cho, G. C. Terahertz imaging with nanometer resolution. *Appl. Phys. Lett.* **2003**, *83*, 3009−3011.

(45) Stinson, H. T.; Sternbach, A.; Najera, O.; Jing, R.; Mcleod, A. S.; Slusar, T. V.; Mueller, A.; Anderegg, L.; Kim, H. T.; Rozenberg, M.; Basov, D. N. Imaging the nanoscale phase separation in vanadium dioxide thin films at terahertz frequencies. *Nat. Commun.* **2018**, *9*, 3604.

(46) Plankl, M.; et al. Subcycle contact-free nanoscopy of ultrafast interlayer transport in atomically thin heterostructures. *Nat. Photonics* **2021**, *15*, 594−600.

(47) Cocker, T. L.; Jelic, V.; Hillenbrand, R.; Hegmann, F. A. Nanoscale terahertz scanning probe microscopy. *Nat. Photonics* **2021**, *15*, 558−569.

(48) Orfanidis, S. J. *Electromagnetic Waves and Antennas*; Rutgers University: Piscataway, New Jersey, 2003.

(49) Yasuda, H.; Hosako, I. Measurement of terahertz refractive index of metal with terahertz time-domain spectroscopy. *Jpn. J. Appl. Phys.* **2008**, *47*, 1632.

(50) Naftaly, M.; Miles, R. E. Terahertz time-domain spectroscopy of silicate glasses and the relationship to material properties. *J. Appl. Phys.* **2007**, *102*, No. 043517.

(51) Jackson, J. D. *Classical electrodynamics*. 3rd ed. (Wiley, Hoboken, NY, 1998).

(52) Pendry, J. B.; Holden, A. J.; Robbins, D. J.; Stewart, W. J. Magnetism from conductors and enhanced nonlinear phenomena. *IEEE Trans. Microwave Theory Technol.* **1999**, *47*, 2075−2084.

(53) Jolliffe, I. T. *Principal Component Analysis*, 2nd ed.; Springer: New York, NY, 2002.

(54) Sibilia, C.; Benson, T. M.; Marciniak, M.; Szoplik, T. *Photonic Crystals: Physics and Technology*; Springer: Milano, 2008.

(55) Sulollari, N.; Keeley, J.; Park, S.; Rubino, P.; Burnett, A. D.; Li, L.; Rosamond, M. C.; Linfield, E. H.; Davies, A. G.; Cunningham, J. E.; Dean, P. Coherent terahertz microscopy of modal field distributions in micro-resonators. *APL Photonics* **2021**, *6*, 66104.

(56) Ozawa, T.; et al. Topological photonics. *Rev. Mod. Phys.* **2019**, *91*, No. 015006.

(57) Yan, Q.; et al. Near-Field Imaging and Time-Domain Dynamics of Photonic Topological Edge States in Plasmonic Nanochains. *Nano Lett.* **2021**, *21*, 9270−9278.

(58) Wu, Q.; Zhang, X.-C. Free-space electro-optic sampling of terahertz beams. *Appl. Phys. Lett.* **1995**, *67*, 3523−3525.

(59) Winnewisser, C.; Jepsen, P. U.; Schall, M.; Schyja, V.; Helm, H. Electro-optic detection of THz radiation in LiTaO3, LiNbO3 and ZnTe. *Appl. Phys. Lett.* **1997**, *70*, 3069−3071.

(60) Wahyudi, T.; Apriono, C.; Zulkifli, F. Y.; Rahardjo, E. T. Broadband planar bow-tie antenna on high resistivity silicon substrate for terahertz application. *15th International Symposium on Electrical and Computer Engineering*; IEEE, 2017; pp 372−376.

(61) Ordal, M. A.; Bell, R. J.; Alexander, R. W.; Long, L. L.; Querry, M. R. Optical properties of fourteen metals in the infrared and far infrared: Al, Co, Cu, Au, Fe, Pb, Mo, Ni, Pd, Pt, Ag, Ti, V, and W. *Appl. Opt.* **1985**, *24*, 4493.

(62) Schneider, J. B. *Understanding the Finite-Difference Time-Domain Method*; School of Electrical Engineering and Computer Science, Washington State University: Pullman, Washington, 2010.